

29. L. Fu, H. Pelicano, J. Liu, P. Huang, C.-C. Lee, *Cell* **111**, 41 (2002).
30. K. Unsal-Kacmaz, T. E. Mullen, W. K. Kaufmann, A. Sancar, *Mol. Cell. Biol.* **25**, 3109 (2005).
31. T. Matsuo *et al.*, *Science* **302**, 255 (2003).
32. N. A. Krucher, L. Meije, M. H. Roberts, *Cell. Mol. Neurobiol.* **17**, 495 (1997).
33. L. E. Anderson, J. E. Morris, L. B. Sasser, R. G. Stevens, *Cancer Lett.* **148**, 121 (2000).
34. J. Hansen, *Epidemiology* **12**, 74 (2001).
35. W. J. Hrushesky, *J. Control. Release* **74**, 27 (2001).
36. G. A. Bjarnason, R. Jordan, *Prog. Cell Cycle Res.* **4**, 193 (2000).
37. www.fgsc.net/fgn47/lgi.htm.
38. S. Gery, N. Komatsu, L. Baldjyan, A. Yu, D. Koo, H. P. Koeffler, *Mol. Cell* **22**, 375 (2006).
39. Supported by grants from the NIH (MH44651 to J.C.D. and J.J.L. and R37GM34985 to J.C.D.), NSF (MCB-0084509 to J.J.L.), and the Norris Cotton Cancer Center core grant to Dartmouth Medical School. We thank R. Rothstein for yeast strain W2105-7b, S. Elledge for plasmid pMH267, and both for helpful discussions.

## Supporting Online Material

www.sciencemag.org/cgi/content/full/1121716/DC1  
Materials and Methods  
Figs. S1 and S2  
References

24 October 2005; accepted 11 May 2006  
Published online 29 June 2006;  
10.1126/science.1121716  
Include this information when citing this paper.

# REPORTS

## Imaging the Mott Insulator Shells by Using Atomic Clock Shifts

Gretchen K. Campbell,<sup>1\*</sup> Jongchul Mun,<sup>1</sup> Micah Boyd,<sup>1</sup> Patrick Medley,<sup>1</sup> Aaron E. Leanhardt,<sup>2</sup> Luis G. Marcassa,<sup>1†</sup> David E. Pritchard,<sup>1</sup> Wolfgang Ketterle<sup>1</sup>

Microwave spectroscopy was used to probe the superfluid–Mott insulator transition of a Bose-Einstein condensate in a three-dimensional optical lattice. By using density-dependent transition frequency shifts, we were able to spectroscopically distinguish sites with different occupation numbers and to directly image sites with occupation numbers from one to five, revealing the shell structure of the Mott insulator phase. We used this spectroscopy to determine the onsite interaction and lifetime for individual shells.

The Mott insulator (MI) transition is a paradigm of condensed matter physics, describing how electron correlations can lead to insulating behavior even for partially filled conduction bands. However, this behavior requires a commensurate ratio between electrons and sites. If this condition for the density is not exactly fulfilled, the system will be conductive. For neutral bosonic particles, the equivalent phenomenon is the transition from a superfluid to an insulator for commensurate densities. In inhomogeneous systems, as in atom traps, the condition of commensurability no longer applies: For sufficiently strong interparticle interactions, it is predicted that the system should separate into MI shells with different occupation number, separated by thin superfluid layers (1–3).

The recent observation of the superfluid-to-MI transition with ultracold atoms (4) has stimulated a large number of theoretical and experimental studies [(5) and references therein]. Atomic systems allow for a full range of control of the experimental parameters, including tunability of the interactions and defect-free preparation, making them attractive systems for studying condensed matter phenomena. The MI

phase in ultracold atoms has been characterized by studies of coherence, excitation spectrum, noise correlations (4, 6, 7), and molecule formation (8). Recently, by using spin-changing collisions, Gerbier *et al.* selectively addressed lattice sites with two atoms and observed the suppression of number fluctuations (9).

In this study, we combined atoms in the MI phase with the high-resolution spectroscopy used for atomic clocks and used density-dependent transition frequency shifts to spectroscopically resolve the layered structure of the Mott shells with occupancies from  $n = 1$  to  $n = 5$  and to directly image their spatial distributions.

Bosons with repulsive interactions in an optical lattice can qualitatively be described by the Hamiltonian (10, 1),

$$\hat{H} = -J \sum_{\langle i,j \rangle} \hat{a}_i^\dagger \hat{a}_j + \frac{1}{2} U \sum_i \hat{n}_i (\hat{n}_i - 1) + \sum_i (\epsilon_i - \mu) \hat{n}_i \quad (1)$$

where the first two terms are the usual Hamiltonian for the Bose-Hubbard model, the last term adds in the external trapping potential, and  $J$  is the tunneling term between nearest neighbors,  $\hat{a}_i^\dagger$  and  $\hat{a}_i$  are the boson creation and destruction operators at a given lattice site.  $U = (4\pi\hbar^2 a/m) \int |w(x)|^4 d^3x$  is the repulsive onsite interaction, where  $\hbar$  is Planck's constant divided by  $2\pi$ ,  $m$  is the atomic mass,  $a$  is the s-wave scattering length,  $w(x)$  is the single particle Wannier function localized to the  $i$ th lattice site, and  $\hat{n}_i = \hat{a}_i^\dagger \hat{a}_i$  is the number operator for bosons

at site  $i$ . The last term in the Hamiltonian is due to the external trapping confinement of the atoms, where  $\epsilon_i = V_{\text{ext}}(r_i)$  is the energy offset at the  $i$ th site due to the external confinement and  $\mu$  is the chemical potential.

The behavior of this system is determined by the ratio  $J/U$ . For low lattice depths, the ratio is large and the system is superfluid. For larger lattice depths, the repulsive onsite energy begins to dominate, and the system undergoes a quantum phase transition to a MI phase. For deep lattices, the atoms are localized to individual lattice sites with integer filling factor  $n$ . This filling factor varies locally depending on the local chemical potential  $\mu_i = \mu - \epsilon_i$  as

$$n = \text{Mod}(\mu_i/U) \quad (2)$$

where  $\text{Mod}$  is the modulo and decreases from the center to the edge of the trap.

To prepare the atoms in the Mott insulating phase, we first created a <sup>87</sup>Rb Bose-Einstein condensate in the the  $|F = 1, m_F = -1\rangle$  state (where  $F$  and  $m_F$  are the quantum numbers for the total spin and its  $t$  component, respectively) by using a combination of an Ioffe-Pritchard magnetic trap and an optical dipole trap. The optical trap was oriented perpendicular to the long axis of the magnetic trap, creating a more isotropic trapping potential that was better matched to the optical lattice. The laser beam for the optical trap had a  $1/e^2$  waist  $\approx 70 \mu\text{m}$  and was retroreflected. However, the polarization of the retroreflected beam was rotated such that the interference between the two beams had minimal contrast. The resulting trap had radial and axial trap frequencies of  $\omega = 2\pi \times 70 \text{ Hz}$  and  $\omega = 2\pi \times 20 \text{ Hz}$ , respectively, where the axial direction is now parallel to the optical trap. A three-dimensional (3D) optical lattice was created by adding two additional retroreflected laser beams derived from the same laser at  $\lambda = 1064 \text{ nm}$ . The lattice was adiabatically ramped up by rotating the polarization of the retroreflected optical trapping beam to increase the interference contrast along that axis and by increasing the laser power in the other two axes. The lattice depth was increased by using an exponential ramp with a 40-ms time constant. After ramping on the lattice, all three beams were linearly polarized orthogonal to each other and

<sup>1</sup>MIT-Harvard Center for Ultracold Atoms, Research Laboratory of Electronics, Department of Physics, Massachusetts Institute of Technology, Cambridge, MA 02139, USA. <sup>2</sup>JILA, Boulder, CO 80309, USA.

\*To whom correspondence should be addressed. E-mail: gcampbel@mit.edu

†Permanent address: Instituto de Física de São Carlos, University of São Paulo, São Paulo 13560-970, Brazil.

had different frequency detunings generated by using acousto-optic modulators. The lattice depth was up to  $40E_{\text{rec}}$ , where  $E_{\text{rec}} = \hbar^2 k^2 / 2m$  is the recoil energy and  $k = 2\pi/\lambda$  is the wave vector of the lattice light. At  $40E_{\text{rec}}$ , the lattice trap frequency at each site was  $\omega_{\text{lat}} = 2\pi \times 25$  kHz, and the external trap frequencies increased to  $\omega = 2\pi \times 110$  Hz and  $\omega = 2\pi \times 30$  Hz in the radial and axial directions, respectively.

Zeeman shifts and broadening of the clock transition from the  $F = 1$  to the  $F = 2$  state were avoided by using a two-photon transition between the  $|1, -1\rangle$  state and the  $|2, 1\rangle$  state, where at a magnetic bias field of  $\sim 3.23$  G both states have the same first-order Zeeman shift (11). The two-photon pulse was composed of one microwave photon at a fixed frequency of 6.83 GHz and one radio frequency (rf) photon at a frequency of around 1.67 MHz. The pulse had a duration of 100 ms, and when on resonance the fraction of atoms transferred to the  $|2, 1\rangle$

state was less than 20%. After the pulse, atoms in the  $|2, 1\rangle$  state were selectively detected with absorption imaging by using light resonant with the  $5^2S_{1/2}|2, 1\rangle \rightarrow 5^2P_{3/2}|3, 1\rangle$  transition. For observing the spatial distribution of the Mott shells, we imaged the atoms in the trap. For recording spectra, we released the atoms from the trap and imaged them after 3 ms of ballistic expansion in order to reduce the column density.

When the two-photon spectroscopy is performed on a trapped condensate without a lattice, the atoms transferred to the  $|2, 1\rangle$  state have a slightly different mean field energy because of the difference between  $a_{21}$  and  $a_{11}$  scattering lengths, where  $a_{21}$  is the scattering length between two atoms in states  $|2, 1\rangle$  and  $|1, -1\rangle$  and  $a_{11}$  is the scattering length between two atoms in the  $|1, -1\rangle$  state. This difference in scattering lengths leads to a density-dependent shift to the resonance frequency,  $\Delta\nu \propto \rho(a_{21} - a_{11})$ , where  $\rho$  is the condensate density (11). This collisional

shift is commonly referred to as the clock shift (12) because of its importance in atomic clocks, where cold collisions currently limit the accuracy (13, 14). When performed on a condensate with peak density  $\rho_0$  in a harmonic trap in the limit of weak excitation, the line shape for the two-photon resonance is given by (15):

$$I(\nu) = \frac{15h(\nu - \nu_0)}{4\rho_0\Delta E} \sqrt{1 - \frac{h(\nu - \nu_0)}{\rho_0\Delta E}} \quad (3)$$

where  $\nu_0$  is the hyperfine transition frequency and the mean field energy difference is

$$\Delta E = \frac{\hbar^2}{\pi m} (a_{21} - a_{11}) \quad (4)$$

In the case of  $^{87}\text{Rb}$ ,  $a_{21} = 5.19$  nm and  $a_{11} = 5.32$  nm (16). Both the frequency shift and the linewidth increase with the condensate density. As the lattice is ramped on, the peak density of the condensate in a given lattice site increases as

$$\rho_0(r) = \left( \mu - \frac{1}{2} m \omega_{\text{trap}}^2 r^2 \right) / U \quad (5)$$

where  $\omega_{\text{trap}}$  is the external trap frequency for the combined magnetic and optical trap, and, by using the Thomas-Fermi approximation  $\mu$ , the chemical potential, is given by

$$\mu = \left[ \frac{15}{16} \frac{(\lambda/2)^3 m^{3/2} N U \omega_{\text{trap}}^3}{\sqrt{2\pi}} \right]^{2/5} \quad (6)$$

where  $N$  is the total atom number. For low lattice depths, the system is still a superfluid, delocalized over the entire lattice. However, the two-photon resonance line is shifted and broadened because of the increased density, with the center of the resonance at  $\nu = \nu_0 + 2\rho_0\Delta E/3h$ . For deep lattices in the MI regime, the repulsive onsite interaction dominates, number fluctuations are suppressed, and each lattice site has a sharp resonance frequency determined by the occupation number in the site. The separation between

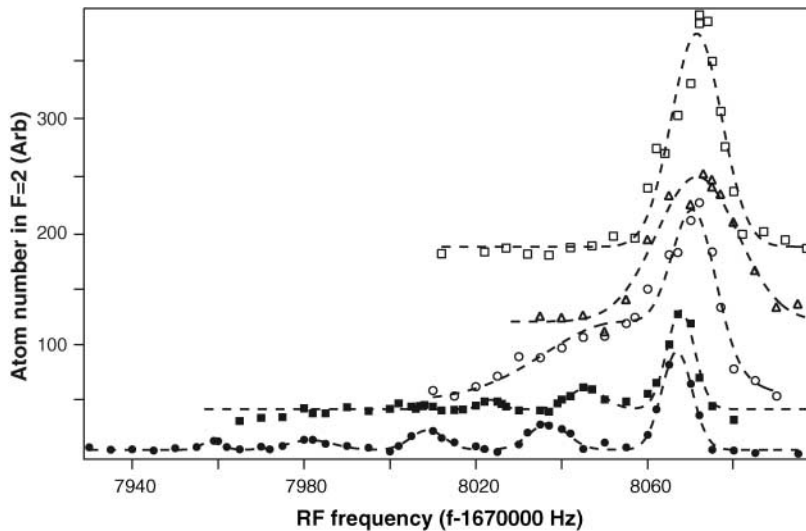
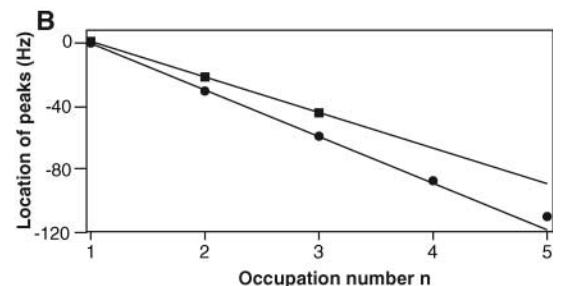
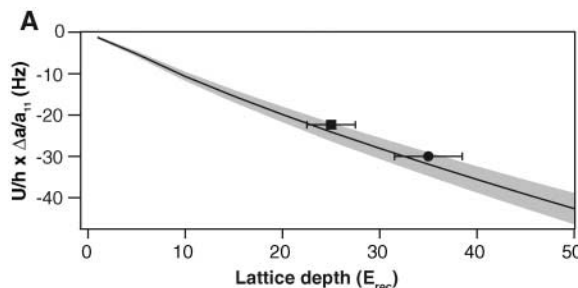


**Fig. 1.** Two-photon spectroscopy across the superfluid-to-MI transition. Spectra for 3D lattice depths of  $0E_{\text{rec}}$  (open squares),  $5E_{\text{rec}}$  (open triangles),  $10E_{\text{rec}}$  (open circles),  $25E_{\text{rec}}$  (solid squares), and  $35E_{\text{rec}}$  (solid circles) are shown. The spectra are offset for clarity. The shift in the center of the  $n = 1$  peak as the lattice depth is increased is due to the differential AC Stark shift from the lattice. The dotted lines show Gaussian fits of the peaks.

**Fig. 2.** Probing the onsite interaction energy.

(A) The separation between the  $n = 1$  and  $n = 2$  peaks is shown for lattice depths of  $V = 25E_{\text{rec}}$  (square) and  $V = 35E_{\text{rec}}$  (circle). As the lattice depth was increased, the separation increased from 22(1) Hz to 30(1) Hz. The shaded

area gives the expected value determined from a band structure calculation, including the uncertainty in the scattering lengths. The uncertainty in the measured separation is indicated by the size of the points. (B) Location of resonances for all MI phases relative to the  $n = 1$  phase for  $V = 25E_{\text{rec}}$  and  $V = 35E_{\text{rec}}$ . For low site occupation ( $n$  values



from 1 to 3), the separation between the resonances is roughly constant, implying constant  $U$ . For  $V = 35E_{\text{rec}}$ , the separation between the  $n = 4$  and  $n = 5$  peaks was 22(2) Hz, a 27% decrease from the 30(1) Hz separation between the  $n = 1$  and  $n = 2$  peaks. The slope of the lines is fit to the separation between the  $n = 1$  and  $n = 2$  peaks.

the resonance frequencies for the  $n$  and  $n - 1$  MI phases is given by

$$\delta\nu = \frac{U}{h}(a_{21} - a_{11})/a_{11} \quad (7)$$

The linewidth of the resonances is no longer broadened by the inhomogeneous density and should be limited only by the bandwidth of the two-photon pulse.

The resonance transitioned from a broadened line to several sharp lines as the lattice depth was increased (Fig. 1). At a lattice depth of  $V = 5E_{\text{rec}}$ , the line was broadened and the line center was shifted slightly because of the increased density. At  $V = 10E_{\text{rec}}$ , the line was shifted and broadened further, and in addition the line shape became asymmetric as the atom number in lattice sites with small occupation was squeezed. For deeper lattice depths, the system underwent a phase transition to a MI phase, and discrete peaks appeared, corresponding to MI phases with different filling factors; for  $V = 35E_{\text{rec}}$ , MI phases with occupancies of up to five were observed.

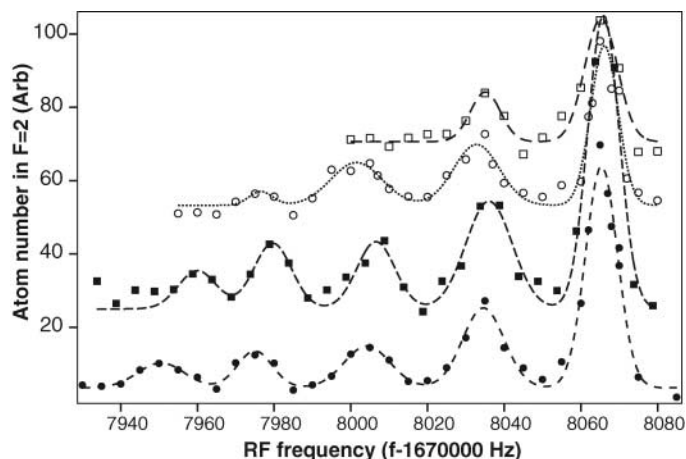
When the lattice depth was increased inside the MI regime (from  $V = 25E_{\text{rec}}$  to  $V = 35E_{\text{rec}}$ ), the separation between the resonance peaks increased, presumably because of the larger onsite interaction energy as the lattice trap was increased. As given in Eq. 7, the separation between the peaks provides a direct measurement of the onsite interaction energy,  $U$ . Our results are in good agreement with calculated values of  $U$  (Fig. 2A). Although the separation between the  $n = 1$ ,  $n = 2$ , and  $n = 3$  peaks is roughly constant, for higher filling factors the separation between the peaks decreases; the effective onsite interaction energy becomes smaller for higher filling factors (Fig. 2B). This result shows that for low occupation numbers the atoms occupy the ground state wave function of the lattice site, whereas for larger occupation numbers, the repulsive onsite interaction causes the wave function to spread out, lowering the interaction energy. From a variational calculation of the wave function similar to (17), we

find that the onsite energy for the  $n = 5$  shell should be  $\sim 20\%$  smaller than that for the  $n = 1$  shell, in agreement with the measured value (Fig. 2B).

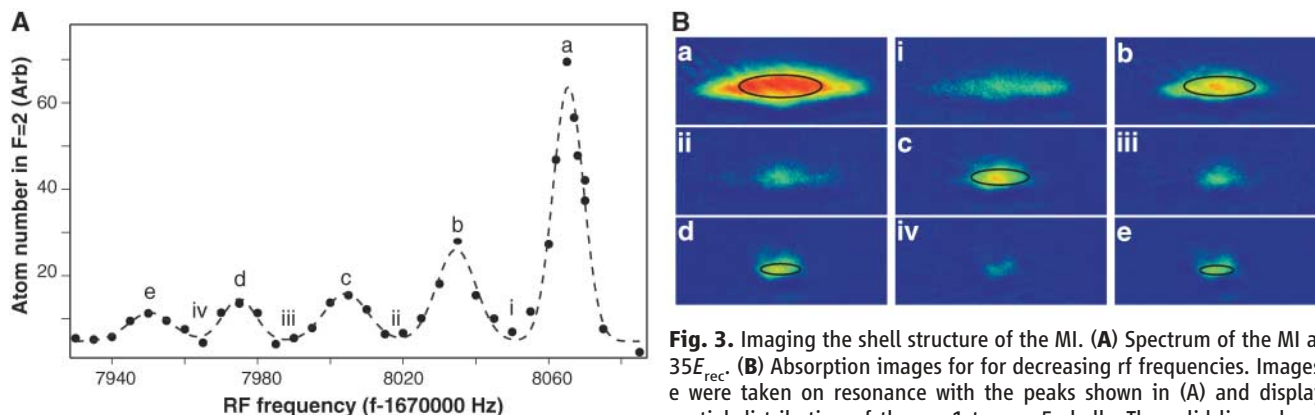
The peaks for the different occupation numbers were spectrally well separated. Therefore, on resonance, only atoms from a single shell were transferred to the  $|2, 1\rangle$  state. An image of these atoms (without any time of flight) shows the spatial distribution of this shell. Figure 3B shows absorption images for  $n = 1$  to  $n = 5$  shells. As predicted (1), the  $n = 1$  MI phase appears near the outer edge of the cloud. For larger  $n$ , the radius of the shell decreases, and the  $n = 5$  sites form a core in the center of the cloud. The expected radius for each shell was obtained from Eq. 2 by using the measured values for the onsite interaction. The observed radii were in good agreement except for the  $n = 1$  shell, which may have been affected by anharmonicities in the external trap. Absorption images taken with rf values between the peaks show a small signal, which may reflect the predicted thin superfluid layers between the insulating shells; however, this needs to be studied further with improved signal-to-noise ratio. The expected absorption

image of a shell should show a column density with a flat distribution in the center and raised edges. However, because of limitations (resolution and residual fringes) in our imaging system, these edges were not resolved.

Because we were able to address the different MI phases separately, we could determine the lifetime for each shell. For this, the atoms were first held in the lattice for a variable time  $\tau$  before applying the 100-ms two-photon pulse. For the  $n = 1$  MI phase and ignoring technical noise, the lifetime should only be limited by spontaneous scattering from the lattice beams. Even for the deepest lattices, the spontaneous scattering rate is less than  $10^{-2}$  Hz. For the  $n = 2$  MI phase, the lifetime is limited by dipolar relaxation, which for  $^{87}\text{Rb}$  is slow, with a rate  $< 10^{-2}$  Hz. For sites with  $n \geq 3$ , the lifetime is limited by three-body recombination with a rate equal to  $\gamma n(n-1)(n-2)$  (18), with  $\gamma = 0.026$  Hz for our parameters. This gives three-body lifetimes of  $\tau_{3B}$  of 6.2 s, 1.6 s, and 0.6 s for the  $n = 3$ ,  $n = 4$ , and  $n = 5$  MI phases, respectively. This calculation of  $\gamma$  assumes for the density distribution the ground state of the harmonic oscillator potential, so for higher filling factors the actual lifetime could be higher. We



**Fig. 4.** Lifetime of individual MI shells. The lifetime for each MI phase can be measured independently by adding a hold time before applying the two-photon pulse. Spectra are shown for hold times of 0 ms (solid circles), 100 ms (solid squares), 400 ms (open circles), and 2000 ms (open squares). The lattice depth was  $V = 35E_{\text{rec}}$  except for the 100-ms hold time, for which it was  $V = 34E_{\text{rec}}$ . The lines show Gaussian fits to the peaks, and the spectra were offset for clarity.



**Fig. 3.** Imaging the shell structure of the MI. (A) Spectrum of the MI at  $V = 35E_{\text{rec}}$ . (B) Absorption images for decreasing rf frequencies. Images a to e were taken on resonance with the peaks shown in (A) and display the spatial distribution of the  $n = 1$  to  $n = 5$  shells. The solid lines show the predicted contours of the shells. Absorption images taken for rf frequencies between the peaks (images i to iv) show a much smaller signal. The field of view was  $185 \mu\text{m}$  by  $80 \mu\text{m}$ .

predicted contours of the shells. Absorption images taken for rf frequencies between the peaks (images i to iv) show a much smaller signal. The field of view was  $185 \mu\text{m}$  by  $80 \mu\text{m}$ .

show relative populations as a function of the hold time and derive lifetimes as  $\tau$  almost equal to 1 s, 0.5 s, and 0.2 s for the  $n = 3$ ,  $n = 4$ , and  $n = 5$  MI phases, respectively (Fig. 4); this is shorter than predicted, which is possibly due to secondary collisions. For  $n = 1$  and  $n = 2$ , lifetimes of over 5 s were observed.

We expect that this method can be used to measure the number statistics as the system undergoes the phase transition. One would expect that the spectral peaks for higher occupation number become pronounced only at higher lattice depth; an indication of this can be seen already in Fig. 1. For low lattice depths, the tunneling rate is still high, but one can suddenly increase the lattice depth and freeze in populations (19), which can then be probed with high-resolution spectroscopy. Fluctuations in the atom number could identify the superfluid layers between the Mott shells. In addition, by applying a magnetic gradient across the lattice, tomographic slices could be selected, combining full 3D resolution with spectral resolution of the site occupancy. These techniques may address questions about local properties that have been raised in recent theoretical simulations (20). The addressability of

individual shells could be used to create systems with only selected occupation numbers (e.g., by removing atoms in other shells). Such a preparation could be important for the implementation of quantum gates, for which homogenous filling is desirable. For atoms other than rubidium, atomic clock shifts are much larger, e.g., for sodium, larger by a factor of 30. Therefore, it should be easier to resolve the MI shells, unless the collisional lifetime of the upper state of the clock transition sets a severe limit to the pulse duration.

*Note added in proof:* After submission of this work, the vertical profile of an  $n = 2$  MI shell was obtained by using spin-changing collisions and a magnetic resonance imaging technique (21).

#### References and Notes

1. D. Jaksch, C. Bruder, J. I. Cirac, C. W. Gardiner, P. Zoller, *Phys. Rev. Lett.* **81**, 3108 (1998).
2. G. G. Batrouni *et al.*, *Phys. Rev. Lett.* **89**, 117203 (2002).
3. B. Marco, C. Lannert, S. Vishveshwara, T. C. Wei, *Phys. Rev. A* **71**, 063601 (2005).
4. M. Greiner, O. Mandel, T. Esslinger, T. W. Hänsch, I. Bloch, *Nature* **415**, 39 (2002).
5. I. Bloch, *Nature Phys.* **1**, 23 (2005).
6. T. Stöferle, H. Moritz, C. Schori, M. Köhl, T. Esslinger, *Phys. Rev. Lett.* **92**, 130403 (2004).

7. S. Fölling *et al.*, *Nature* **434**, 481 (2005).
8. T. Volz *et al.*, published online 8 May 2006 (<http://arxiv.org/abs/cond-mat?paperum=0605184>).
9. F. Gerbier, S. Fölling, A. Widera, O. Mandel, I. Bloch, *Phys. Rev. Lett.* **96**, 090401 (2006).
10. M. P. A. Fisher, P. B. Weichman, G. Grinstein, D. S. Fisher, *Phys. Rev. B* **40**, 546 (1989).
11. D. M. Harber, H. J. Lewandowski, J. M. McGuirk, E. A. Cornell, *Phys. Rev. A* **66**, 053616 (2002).
12. K. Gibble, S. Chu, *Phys. Rev. Lett.* **70**, 1771 (1993).
13. C. Fertig, K. Gibble, *Phys. Rev. Lett.* **85**, 1622 (2000).
14. Y. Sortais *et al.*, *Phys. Scr.* **195**, 50 (2001).
15. J. Stenger *et al.*, *Phys. Rev. Lett.* **82**, 4569 (1999).
16. E. G. M. van Kempen, S. J. J. M. F. Kokkelmans, D. J. Heinzen, B. J. Verhaar, *Phys. Rev. Lett.* **88**, 093201 (2002).
17. G. Baym, C. J. Pethick, *Phys. Rev. Lett.* **76**, 6 (1996).
18. M. W. Jack, M. Yamashita, *Phys. Rev. A* **67**, 033605 (2005).
19. M. Greiner, O. Mandel, T. W. Hänsch, I. Bloch, *Nature* **419**, 51 (2002).
20. O. Gygi, H. G. Katzgraber, M. Troyer, S. Wessel, G. G. Batrouni, *Phys. Rev. A* **73**, 063606 (2006).
21. S. Fölling, A. Widera, T. Mueller, F. Gerbier, I. Bloch, published online 23 June 2006 (<http://arxiv.org/abs/cond-mat?paperum=0606592>).
22. The authors thank I. Bloch and S. Fölling for insightful discussions. This work was supported by NSF. L.G.M. also acknowledges support from Fundação de Apoio a Pesquisa do Estrado de São Paulo.

23 May 2006; accepted 7 July 2006  
10.1126/science.1130365

## Evidence for a Past High-Eccentricity Lunar Orbit

Ian Garrick-Bethell,\* Jack Wisdom, Maria T. Zuber

The large differences between the Moon's three principal moments of inertia have been a mystery since Laplace considered them in 1799. Here we present calculations that show how past high-eccentricity orbits can account for the moment differences, represented by the low-order lunar gravity field and libration parameters. One of our solutions is that the Moon may have once been in a 3:2 resonance of orbit period to spin period, similar to Mercury's present state. The possibility of past high-eccentricity orbits suggests a rich dynamical history and may influence our understanding of the early thermal evolution of the Moon.

The Moon is generally thought to have accreted close to the Earth and migrated outward in a synchronously locked low-eccentricity orbit. During the early part of this migration, the Moon was cooling and continually subjected to tidal and rotational stretching. The principal moments of inertia  $A < B < C$  of any satellite are altered in a predictable way by deformation due to spin and tidal attraction. The moments are typically characterized by ratios that are easier to measure, namely, the libration parameters  $\beta = (C - A)/B$  and  $\gamma = (B - A)/C$ , and the degree-2 spherical-harmonic gravity coefficients  $C_{20} = (2C - B - A)/(2Mr^2)$  and  $C_{22} = (B - A)/(4Mr^2)$ , where  $M$  and  $r$  are the satellite mass and radius. Of these four values

$\beta$ ,  $\gamma$ , and  $C_{20}$  can be taken as independent. Using the ratio  $(C - A)/A$ , Laplace was the first to observe that the lunar moments are not in equilibrium with the Moon's current orbital state (1). He did not, however, address the possibility of a "fossil bulge," or the frozen remnant of a state when the Moon was closer to the Earth. Sedgwick examined the lunar moments in 1898, as did Jeffreys in 1915 and 1937, and both authors effectively showed that  $\beta$  is too large for the current orbit, suggesting that the Moon may carry a fossil bulge (2–5). However, Jeffreys showed that the fossil hypothesis might be untenable because the ratio of  $\gamma/\beta = 0.36$  does not match the predicted ratio of 0.75 for a circular synchronous orbit (equivalently,  $C_{20}/C_{22} = 9.1$ , instead of the predicted ratio of 3.33). Indeed, using data from (6), none of the three independent measures of moments represent a low-eccentricity synchronous-orbit hydrostatic form;  $C_{20} = 2.034 \times 10^{-4}$  is 22 times too large for the current state, and  $\beta =$

$6.315 \times 10^{-4}$  and  $\gamma = 2.279 \times 10^{-4}$  are 17 and 8 times too large, respectively (7, 8).

The inappropriate ratio of  $\gamma/\beta$  or  $C_{20}/C_{22}$  has led some to dismiss the fossil bulge hypothesis as noise due to random density anomalies (9, 10). However, the power of the second-degree harmonic gravity field is anomalously high when compared to the power expected from back extrapolating the power of higher harmonics (7, 11). This suggests that the bulge may be interpreted as a signal of some process. Degree-2 mantle convection has been proposed as a means of deforming the Moon (12, 13), but the dissimilarity of all three principal moments violates the symmetry of any simple degree-2 convection model (12). The Moon's center-of-mass/center-of-figure offset influences the moment parameters slightly, but that problem is geophysically separate and mathematically insignificant to the degree-2 problem (8, 14).

Because  $C_{20}$  is due primarily to rotational flattening, and  $C_{22}$  is due to tidal stretching, the high  $C_{20}/C_{22}$  ratio seems to imply that the Moon froze in its moments while rotating faster than synchronous. However, in such cases no constant face would be presented to the Earth for any  $C_{22}$  power to form in a unique lunar axis. This apparent dilemma can be avoided by considering that in any eccentric orbit with an orbit period to spin period ratio given by  $n:2$ , with  $n = 2, 3, 4, \dots$ , the passage through pericenter results in higher  $C_{22}$  stresses throughout a single elongated axis (hereafter called the pericenter axis). When the stresses experienced over one orbit period are time-averaged, the highest stresses

Department of Earth, Atmospheric and Planetary Sciences, Massachusetts Institute of Technology, 77 Massachusetts Avenue, Cambridge, MA 02139, USA.

\*To whom correspondence should be addressed. E-mail: iang@mit.edu